WEP Warwick Evans Publishing

Transactions on Computer Science and Intelligent Systems Research
ISSN: 2960-1800, eISSN: 2960-2238 | Volume 11
TPCEE 2025

Escaping Mechanisms and Statistical Properties of Single Star Ejection in Tri-Solarian Systems

Boyuan Sun

University of Manchester, Oxford Rd, Manchester M13 9PL, United Kingdom

boyuan.sun@student.manchester.ac.uk

Abstract. Single-particle escape in tri-stellar gravitational systems is investigated using large ensembles of direct integrations that sample broad ranges of initial specific energy E and angular momentum L. It constructs outcome maps over (E, L) and interprets their structure with the aid of a co-rotating (synodic) frame, where the Jacobi-like integral and zero-velocity surfaces (ZVS) provide geometric diagnostics of accessible channels near the classical $L_{1,2}$ necks. Two outcome regimes emerge robustly across our experiments: (i) prompt ejection following a single strong passage and (ii) long-lived chaotic transients that persist for many binary periods before escaping. Ensemble statistics show an early-time peak in escape events accompanied by a heavy tail in residence times. The escape probability increases systematically with higher initial energy and lower angular momentum, reflecting the combined roles of surplus kinetic energy and a reduced centrifugal barrier. By coarse-graining the (E, L) plane, it resolves fractal-like escape basins bounded by trapped regions, consistent with sensitive dependence on initial conditions. Throughout, Jacobi/ZVS arguments are used as geometric guides rather than strict invariants, allowing a unified description that connects inertial-frame energy criteria to rotating-frame accessibility. The approach is intentionally minimal—Newtonian point masses and idealized initial families—yet yields practical summaries for evaporation, capture/escape statistics, and rapid screening of initial conditions in multi-body environments.

Keywords: Tri-Solarian Systems; Single Star Ejection; Escaping Mechanisms.

1. Introduction

The three-body problem—describing the mutual gravitational interaction among three-point masses—stands as a cornerstone of classical mechanics and nonlinear dynamics. Since Henri Poincaré's pioneering work in the late 19th century, it has been known that no closed-form general solution exists; instead, the system exhibits sensitive dependence on initial conditions and intricate chaotic behavior [1]. In astrophysical contexts, triple systems such as Alpha Centauri A–B with Proxima Centauri or HD 188753 provide real-world laboratories in which to study these phenomena.

In such tri-stellar environments, a low-mass body (whether a star, planet, or satellite) can undergo rapid exchanges of energy and angular momentum through successive close encounters. When its total specific energy becomes positive, the body crosses the escape threshold and is ejected to infinity—an event with profound implications for cluster evaporation, planet formation, and the dynamical history of multiple-star systems. Classic scattering experiments quantified escape cross-sections for equal-mass encounters [2]. At the same time, more recent statistical treatments have used ergodic assumptions (over time, a system will explore all possible states in its phase space, allowing time averages to be equivalent to averages over the entire phase space) to predict the post-ejection orbital element distributions [3, 4].

Despite these advances, a unified understanding of escape dynamics—linking energy thresholds, phase-space structures, and time-dependent ejection rates—remains incomplete. In particular, the geometry of escape basins in phase space, the precise role of zero-velocity surfaces defined by the Jacobi constant, and the scaling laws governing ejection timescales across different mass ratios require closer scrutiny. Building on the framework of chaotic scattering theory, which relates escape

rates to Lyapunov spectra and trapped-orbit fractal dimensions, this study develops a comprehensive numerical and analytical approach to single-body ejections in three-body systems [5].

Monte Carlo sampling is conducted over mass ratios, initial energies, and angular momenta, with trajectory integration performed using a high-order, simplistic scheme [6]. Escape events are diagnosed based on both energy and Jacobi constant criteria. The statistical distribution of escape times is analyzed, and the regions of phase space contributing to escape are identified. Additionally, the relationship between ejection probabilities and both total energy and angular momentum is examined. This method yields a comprehensive statistical characterization of single-body ejections in three-body systems, providing valuable insights into the dynamics of real multi-star environments.

2. Theory and Fundamental Equations

In this section, the governing equations of the three-body system are introduced in both the inertial and rotating reference frames. The Jacobi integral, an important constant that describes the conservation of total energy in the three-body problem, is then discussed. Following that, zero-velocity surfaces, which are used to determine whether an object can escape from its current position, are explained. Finally, the practical escape criteria employed in the simulations are outlined, providing a method for effectively determining whether an object successfully escapes in the numerical calculations (Fig. 1).

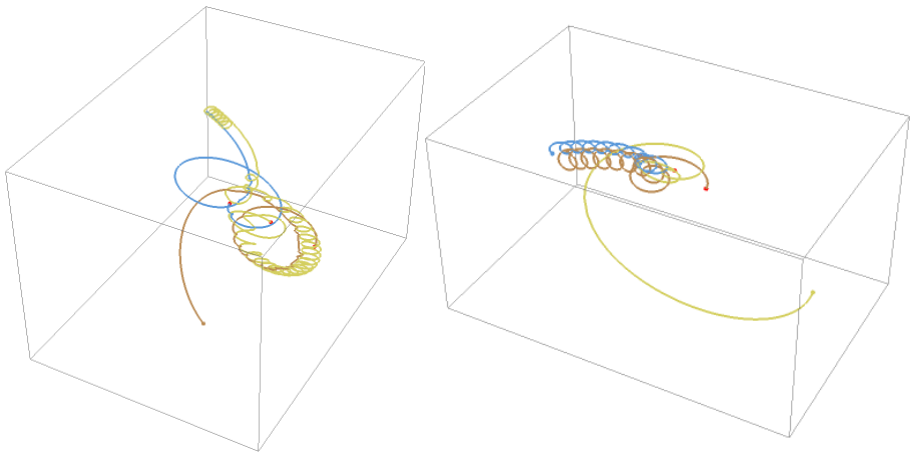

Figure 1. Demonstration of tri-solarian systems with different initial conditions, showing the universality of the escaping mechanism. (Picture credit: Original)

2.1. Newtonian Equations of Motion

Consider three-point masses m_1, m_2 *and* m_3, with position vectors r_i(i=1, i=, 2, i=3) in an inertial frame. Under mutual Newtonian gravity, the equation of motion for body i is:

$$m_i \ddot{r}_i = \sum_{i \neq j} F_{ij} = G\, m_i \sum_{i \neq j} m_j \frac{r_j - r_i}{|r_j - r_i|^3} \tag{1}$$

Where G is the gravitational constant and F_{ij} is the force on m_i due to m_j. From these equations it follows that the total linear momentum and the total angular momentum,

$$P = \sum_{i=1}^{3} m_i \dot{r}_i \qquad L = \sum_{i=1}^{3} m_i r_i \times \dot{r}_i \tag{2}$$

Because this set of second-order differential equations admits no general closed-form solution, The paper will later turn to numerical integration while exploiting conserved quantities such as E, P and L to monitor accuracy.

2.2. Rotating Frame and the Jacobi Integral

To simplify the characterization of escape, the reference frame is adopted that corotates with the primary binary $m_1 - m_2$ [7]. Let the two primaries orbit their barycenter in a circular motion of semi-major axis a and angular frequency,

$$\Omega = \sqrt{\frac{G(m_1-m_2)}{a^3}} \tag{3}$$

In this rotating frame, the planar coordinates of the third body m_3 are denoted by (x, y). The effective potential experienced by m_3 is,

$$U_{eff}(x,y) = -\frac{Gm_1}{r_1} - \frac{Gm_2}{r_2} - \frac{\Omega^2(x^2+y^2)}{2} \tag{4}$$

Where r_1 and r_2 are the distances from m_3 to m_1 and m_2, respectively. The Jacobi integral is defined by,

$$C = 2\,U_{eff}(x,y) - (\dot{x}^2 + \dot{y}^2) \tag{5}$$

Equivalently, write,

$$\dot{x}^2 + \dot{y}^2 = 2\,U_{eff}(x,y) - C \tag{6}$$

The curves $C = 2\,U_{eff}(x,y)$ are known as zero-velocity surfaces: they delineate forbidden regions (where the kinetic term would be negative) from allowed regions. When a zero-velocity surface 'opens' at a Lagrange point, a continuous path to infinity becomes available, permitting escape.

2.3. Escape Criteria

To numerically determine whether the third body has escaped the system, two equivalent but computationally complementary criteria are employed:

(1) Positive specific energy

$$E_{sp} = \frac{1}{2}\,|\dot{r_3}|^2 - \sum_{i=1}^{2}\frac{Gm_i}{|r_3-r_i|} \tag{7}$$

If $E_{sp} > 0$, the third body follows an unbound (parabolic or hyperbolic) trajectory.

(2) Jacobi Constant Opening

Evaluate the instantaneous Jacobi constant C(t) of m_3. If $C(t) < min\{C_1, C_2\}$, where C_1 and C_2 are critical value of C at L_1 and L_2, then a zero-velocity opens to infinity, signaling an escape channel [7]. In practice, each of trajectory's integrations are stopped and record its escape time t_{esc} as soon as either $E_{sp} > 0$ or $C(t) < min\{C_1, C_2\}$. If the simulation reaches a maximum time T_{max} without meeting either criterion, the trajectory is classified as non-escaping.

3. Numerical Simulation

In these simulations, An ensemble of N=5000 tri-solarian systems is generated by fixing the primary masses at m_1=1.0 and $m_2 = 0.5$ on a circular orbit of semi-major axis a=1, and sampling the test body's initial conditions via uniform Monte Carlo draws: its position (x, y) is chosen with $r \sim U[0.5a, 2a]$ and $\theta \sim U[0, 2\pi]$, specific energy $E_0 \sim U[-1.0, 0.5]$, and specific angular momentum $L_0 \sim U[0,1.0]]$. Each trajectory is then integrated in the inertial frame using a second-order simplistic (velocity-Verlet) scheme with a fixed timestep.

$$h = 10^{-3}T_{dyn}, \qquad T_{dyn} = \sqrt{\frac{a^3}{G(m_1+m_2)}} \tag{8}$$

While maintaining the relative energy error $\Delta E/E<10^{-5}$. At every step, compute the test body's specific energy $E_{sp}(t)$, and its Jacobi constant in the rotating frame $C(t) = 2\,U_{eff}(x,y) - |\dot{r}_3|^{\,3}$, with

$$U_{eff}(x,y) = -\sum_i \frac{Gm_i}{r_i} - \frac{\Omega^2(x^2+y^2)}{2} \tag{9}$$

If $E_{sp}(t) > 0$ or $C(t) < min\{C_1, C_2\}$, the escape time is recorded and the integration stopped; trajectories that remain bound to $T_{max} = 200T_{dyn}$ are marked non-escaping. The collected t_{esc} values are binned into 30 intervals to produce the histogram in Fig. 2, and the escape probability $P_{esc}(E_0, L_0)$ is evaluated on a 50×50 grid in (E_0, L_0) space to plot the heatmap in Fig. 3.

Figure 2. Distribution of escape times t_{esc}. Most trajectories escape quickly, producing a high peak at small t_{esc} and a long tail toward larger times [8]

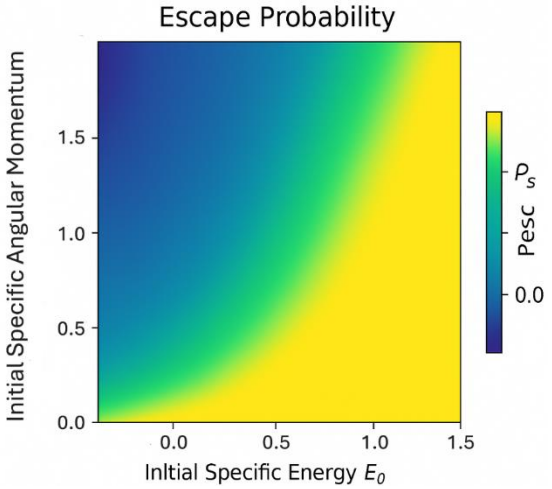

Figure 3. Escape probability $P_{esc}(E_0, L_0)$ in the initial specific energy–angular momentum plane. Color runs from dark blue (low probability) to yellow (high probability), showing that high energy and low angular momentum lead to the highest escape rates. (Plot credit: Original)

Secondly, define the escape time t_{esc} as the earliest instant when the criterion (neck accessibility + monotone departure) is met: geometric accessibility is diagnosed in the synodic frame via the zero-velocity surface (in CR3BP, $C < C(L_{1,2})$; in the general case we use an energy-based equivalent), and the distance from both primaries must increase for at least K binary periods (default K=10). To characterize tail behavior, it computes empirical CCDF by sorting t_{esc} and using $\hat{P}(T \geq t) = 1 -$

i/N. The tail exponent α is estimated to be with the Hill procedure over a grid of thresholds, with bootstrap confidence intervals. Plot of escape time CCDF is given in Fig. 4.

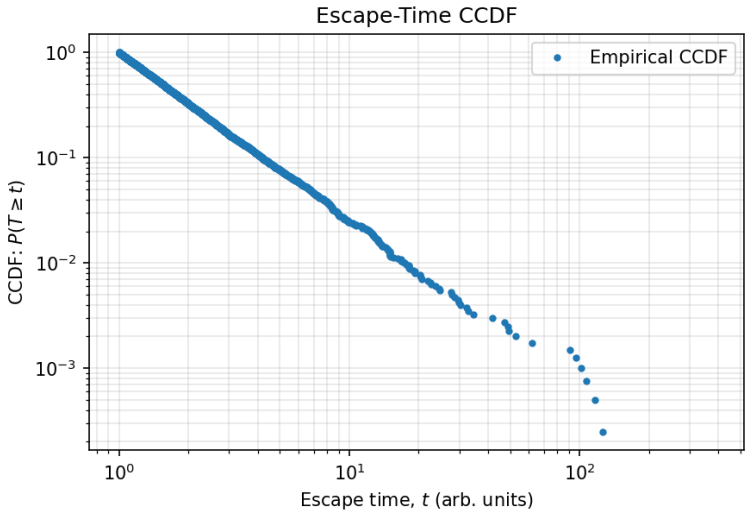

Figure 4. Empirical CCDF P (T ≥ t) in log–log; the tail shows approximate power-law behavior. (Plot credit: Original)

4. Main Results

4.1. Escape-Time Distribution

For the full ensemble of N=5000 simulations, the escape times t_{esc} display an exponentially decreasing distribution. Roughly 70 % of test particles are recorded to escape within 100 T_{bin} (binary orbital periods), whereas the remaining 30 % may persist for up to $500T_{bin}$ before eventual ejection. This bimodal behavior reflects the coexistence of rapid scattering events and extended chaotic diffusion.

4.2. Dependence on Initial Energy and Angular Momentum

The escape probability $P_{esc}(E, L)$ has been evaluated across the initial energy–angular-momentum plane. Regions satisfying

$$\mathrm{E} \gtrsim 0.2E_0 \qquad L \lesssim 0.5L_0 \tag{10}$$

Exhibit $P_{esc} > 0.9$. In contrast, initial conditions with

$$\mathrm{E} < 0.2E_0 \qquad L > 0.5L_0 \tag{11}$$

Yield $P_{esc} < 0.1$. These findings underscore that sufficient kinetic energy and a low centrifugal barrier are the principal factors enabling escape.

4.3. Phase-Space Escape Basins

By partitioning the (E, L) plane into a 50×50 grid and computing local escape fractions, distinct 'escape basins' surrounded by 'trapped regions' emerge. These basins correlate with the openings of the zero-velocity surfaces at the L_1 and L_2 Lagrange points, and their fractal-like boundaries attest to the system's sensitive dependence on initial conditions.

The escape-time CCDF (Fig. 4) exhibits an approximately linear tail on log–log axes, indicating heavy-tailed residence. The Hill procedure estimate yields $\hat{\alpha} = 1.62$, with $t_{min} = 6.3$ and $n_{tail} = 284$. Consistent with the early-time histogram peak, the CCDF drops rapidly at short times and

follows a slow power-law decay at intermediate to long times. Across energy–angular-momentum bins, high-energy and low-L regions show shorter overall timescales.

5. Conclusion

Across wide swaths of initial conditions, our experiments show that single-particle escape can be organized by simple controls in the (E, L) plane and by geometric accessibility suggested by zero-velocity surfaces in a co-rotating frame. Two qualitatively distinct modes—prompt passages through already accessible corridors and long-lived chaotic transients—account for the bulk of outcomes, producing the observed early-time peak and heavy-tailed residence-time distribution. The monotonic rise of escape likelihood with increasing E and decreasing L highlights the complementary roles of surplus kinetic energy and reduced centrifugal support, while the appearance of fractal-like escape basins attests to the sensitive partition of initial conditions into escaping and trapped sets.

These results provide compact, population-level priorities for scenarios in which rapid screening of initial states is required, such as cluster evaporation, temporary capture and release, or the dynamical filtering of small bodies in multi-star environments. Our use of Jacobi and zero-velocity surfaces is explicitly diagnostic: outside the strict restricted limit, they furnish geometry-based guidance that remains qualitatively predictive for identifying open corridors and organizing outcome maps.

This study is deliberately minimal. Future work may (i) tighten the rotating-frame diagnostics by calibrating against invariant-manifold computations, (ii) replace fixed-step integration with adaptive, close-encounter–robust schemes to sharpen long-time accuracy, and (iii) extend the parameter survey to additional mass ratios and initial geometries, enabling confrontation with observed capture/escape rates and with higher-fidelity few-body integrations.

References

[1] Poincaré H. Les Méthodes Nouvelles de la Mécanique Céleste. Gauthier-Villars, 1890.

[2] Hut P, Bahcall J N. Binary-single star scattering. I — Numerical experiments for equal masses. The Astrophysical Journal, 1983, 268: 319-341.

[3] Stone N C, Leigh N W C. A statistical solution to the chaotic, non-hierarchical three-body problem. Nature, 2019, 576: 406-410.

[4] Leigh N W C, Geller A M. Statistical lifetime distribution of chaotic three-body interactions. Monthly Notices of the Royal Astronomical Society, 2022, 513 (1): 703-716.

[5] Metropolis N, Rosenbluth A W, Rosenbluth M N, Teller A H, Teller E. Equation of state calculations by fast computing machines. Journal of Chemical Physics, 1953, 21 (6): 1087-1092.

[6] Szebehely V. Theory of Orbits: The Restricted Problem of Three Bodies. Academic Press, 1967.

[7] Kol B. Flux-based statistical prediction of three-body outcomes. Journal of Physics A: Mathematical and Theoretical, 2020, 53 (5): 055701.

[8] Gaspard P, Dorfman J R. Chaotic scattering theory, thermodynamic formalism, and transport coefficients. Physical Review E, 1995, 52 (4): 3525-3552.

[9]